RAA 2014 Vol. **14** No. **12**, 1642–1653 doi: 10.1088/1674–4527/14/12/012
http://www.raa-journal.org *http://www.iop.org/journals/raa*

Research in Astronomy and Astrophysics

Echo simulation of lunar penetrating radar: based on a model of inhomogeneous multilayer lunar regolith structure *

Shun Dai[1], Yan Su[1], Yuan Xiao[1,2], Jian-Qing Feng[1,2], Shu-Guo Xing[1,2] and Chun-Yu Ding[1,2]

[1] Key Laboratory of Lunar and Deep Space Exploration, National Astronomical Observatories, Chinese Academy of Sciences, Beijing 100012, China; *dais@nao.cas.cn*
[2] University of Chinese Academy of Sciences, Beijing 100049, China

Received 2014 August 10; accepted 2014 September 13

Abstract Lunar Penetrating Radar (LPR) based on the time domain Ultra-Wideband (UWB) technique onboard China's Chang'e-3 (CE-3) rover, has the goal of investigating the lunar subsurface structure and detecting the depth of lunar regolith. An inhomogeneous multi-layer microwave transfer inverse-model is established. The dielectric constant of the lunar regolith, the velocity of propagation, the reflection, refraction and transmission at interfaces, and the resolution are discussed. The model is further used to numerically simulate and analyze temporal variations in the echo obtained from the LPR attached on CE-3's rover, to reveal the location and structure of lunar regolith. The thickness of the lunar regolith is calculated by a comparison between the simulated radar B-scan images based on the model and the detected result taken from the CE-3 lunar mission. The potential scientific return from LPR echoes taken from the landing region is also discussed.

Key words: Moon — techniques: radar astronomy — methods: numerical

1 INTRODUCTION

Lunar regolith, as part of the lunar subsurface which is composed of tiny, sticky particles that form dusty material less than 1 mm in size, covers a layer on the surface of the Moon. The structure of the debris is unconsolidated, and is mainly composed of clastic rock, powder, breccia and molten glass. The thickness of the regolith varies between $4 \sim 5$ m in areas with lunar mare, and up to 20 m for the oldest surfaces in the lunar highlands (Heiken et al. 1991). Regolith is formed from the constant bombardment of the lunar surface by space weathering processes, including most prominently meteoroid impacts. Such impacts (ranging in size from meters to kilometers) pulverize and mix any exposed rock on the surface. This process occurs at a rate of about 1 mm of regolith production per million years, though it is likely that regolith production was faster in the past due to an increased impactor flux. Therefore, exploring the stratigraphic and tectonic characteristics of lunar regolith helps researchers to better understand the formation and evolution of the Moon.

Radar is a very useful method that takes advantage of radio pulses to image the underlying subsurface of the regolith. The first map containing information about the thickness of the regolith

* Supported by the National Natural Science Foundation of China.

layer was obtained using radar from Arecibo with a 70 cm wavelength and a model that incorporated multiple scattering. This model was applied to the layer on the nearside of the Moon and was used to compare independent estimates for the thickness of regolith layer at landing sites that were visited in the past and other areas (Shkuratov & Bondarenko 2001). Observations with the Lunar Radar Sounder (LRS) onboard of the Japanese Kaguya spacecraft (SELENE) found that most nearside maria have subsurface stratifications (Ono et al. 2009; Kobayashi et al. 2010; Kobayashi et al. 2012). The Chang'e-1 microwave radiometer (Fa & Jin 2007) and the Mini-SARs (Spudis et al. 2010) onboard Chandrayaan-1 and Lunar Reconnaissance Orbiter (LRO) (Nozette et al. 2010) were utilized to study stratigraphic features in lunar subsurface structure. Early observation data have not only been applied to investigate the local/global regolith thickness (Fa & Jin 2010a), but were also utilized in studies of the deep subsurface tectonic structure (Ono et al. 2009).

Ground Penetrating Radar (GPR) and the radar sounder techniques were recently employed in the exploration of the Moon. Kobayashi et al. (2002a,b) applied a two-layer model to simulate an A-scope and B-scan of LRS echoes for lunar maria and highland regions. Fa & Jin (2010b) conducted a numerical simulation of radar echoes that can find demixing in deep lunar subsurfaces. Many GPR data modeling codes have been developed (Bourgeois & Smith 1996; Carcione 1996; Rejiba et al. 2003). The GprMax suite of programs, which incorporates finite differences in time domain modeling, is capable of simulating application scenarios that occur almost daily in GPR (Giannopoulos 2005; Sanintenoy et al. 2008).

In Section 2, the performance of Lunar Penetrating Radar (LPR) is first introduced. Then in Section 3, a multilayer microwave transfer inverse-model for lunar regolith is established. The velocity of propagation, the reflection, refraction and transmission coefficients at the interfaces, the resolution and the dielectric constant of the lunar regolith are also discussed. In Section 4, the model is further used to numerically simulate and analyze variations in echoes obtained from the LPR with implied information about time, location and thickness of the lunar regolith. The thickness of lunar regolith is calculated by comparison between the simulated radar B-scan images based on the model and data collected with the LPR second channel during the Chang'e-3 (CE-3) lunar mission. The potential scientific return from LPR echoes taken from the landing site is also discussed. Discussions are provided in Section 5 and conclusions are given in Section 6.

2 LUNAR PENETRATING RADAR

The CE-3 rover is designed to explore an area of 3 km^2 during its 3-month lifetime, with a maximum traveling distance of 10 km. The LPR onboard of the rover, similar to GPR, is the first instrument to operate on the lunar surface which utilizes the Ultra-Wideband (UWB) impulse technique. This has the goal of detecting the topography of a specific area and the subsurface geological structure in detail (Fang et al. 2014).

The LPR transmits nanosecond pulses in time domain patterns with no carrier frequency. Echoes will be produced at interfaces in the medium as the signal propagates through the deep subsurface layers of the regolith. These echoes are then received and identified by the LPR. Based on the analysis of radar echo signals, the thickness of regolith and subsurface structure may be obtained. Compared to a microwave radiometer, LPR, using an active detection method, can identify impedance variations, which makes results about lunar subsurface imaging more intuitive. Compared to ground-based radars and LRS, the performance of LPR directly transmitted from the lunar surface, with less interference from the space environment, enables greater probing depth and accuracy when measuring lunar subsurface structure.

In order for LPR to detect both the thickness of regolith and the geological structure in the subsurface of the regolith, the LPR incorporates two detection channels: the first one is designed to detect the structure of the shallow region of lunar crust; the center frequency of the transmitted unipolar pulse signal is 60 MHz. The second channel is designed to detect the thickness of lunar

Table 1 LPR Performance

Parameter	Channel 1 Performance	Channel 2 Performance
Transmitter Impulse Voltage (V)	1000	400
Transmitter Repetition Frequency (kHz)	0.5, 1, 2	5, 10, 20
Transmitter Impulse Rising Time (ns)	≤ 5	≤ 1
Receiver Working Frequency (MHz)	$10 \sim 300$	$100 \sim 1000$
Receiver Sample rate (MHz)	400	3200
Receiver Input Dynamic Range (dB)	90	90
Antenna Center Frequency (MHz)	60	500
Antenna Bandwidth (MHz)	≥ 40	≥ 450
Antenna VSWR	≤ 3	≤ 2.5
System Gain (dB)	152	133.3
Probing Depth (m)	≥ 100	≥ 30
Thickness Resolution	1 m	30 cm

regolith; the center frequency of the transmitted bipolar pulse signal is 500 MHz. At 500 MHz, LPR is able to survey a depth range of 30 m in the lunar regolith with a range resolution of < 30 cm, and at 60 MHz, LPR can reach 100 m with a range resolution of < 1 m in the shallow region of lunar crust. In this paper, the emphasis mainly focuses on shallow structure under the lunar surface; the second data channel at 500 MHz is applicable.

The LPR is designed to transmit pulses and receive echo signals when the rover moves, and the scientific data can be sent back when the rover is stationary. There are one transmitting dipole and one receiving dipole for the first channel, which are installed at the back of the rover. There are one transmitting bow tie antenna and two receiving bow tie antennas marked A and B, which are installed at the bottom of the rover. The main technical parameters for the LPR are listed in Table 1.

3 STRUCTURE MODEL FOR LUNAR REGOLITH

3.1 Multilayer Model to Describe Lunar Regolith

The lunar regolith layer and the sputtered layer may have undergone superposition and dislocation as a result of billions of years of erosion, impact, bombardment by meteoroids and effects from radiation. The regolith structure can have inhomogeneous stratifications (Heiken et al. 1991).

Figure 1 shows a simple lunar subsurface structure model for the mare basalt area used in this simulation. The upper medium is the vacuum of free space, with a permittivity of ε_0 and electrical conductivity of σ_0; the second layer which is assumed to be regolith has a finite thickness (ε_1, σ_1); the third layer is filled with ejecta from accumulations of material resulting from crater sputtering (ε_2, σ_2); and the bottom layer is bedrock (ε_3, σ_3). The relative magnetic permeability is assumed to be the same for all four layers and equal to 1.

3.2 Wave Properties

For homogeneous and isotropic materials, the propagation velocity, v, the attenuation coefficient, α, and the electromagnetic (EM) impedance, Z, can be expressed as (Daniels 2004)

$$v = \frac{c}{\sqrt{\varepsilon \cdot \mu}}, \tag{1}$$

$$\alpha = \sqrt{\frac{\mu}{\varepsilon}} \cdot \frac{\sigma}{2}, \tag{2}$$

$$Z = \sqrt{\frac{\mu}{\varepsilon}}, \tag{3}$$

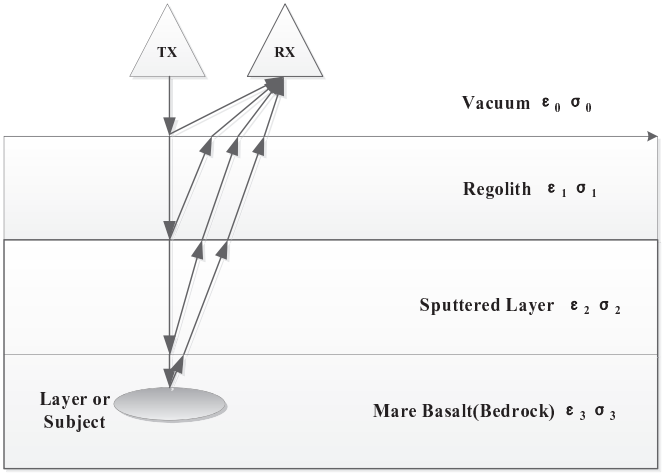

Fig. 1 Simple model for the structure of the lunar subsurface.

where c is the speed of light in a vacuum, μ is the magnetic permeability, ε is the relative dielectric permittivity and σ is the dielectric conductivity. The depth is then derived from

$$d = v \cdot \frac{t}{2}\,, \tag{4}$$

where t is the transit time which is spent to and from the target.

3.3 Electromagnetic Propagation at Interfaces

The LPR antenna maintains a certain distance from the lunar surface, and receives the reflected or scattered signals from the target. The transmitted signal spreads in a vacuum and then into the lunar regolith, and the propagation of reflected signals within the Moon can be modeled as EM wave propagation in layered media. The reflection coefficients of a plane wave at the interface between lunar layers i and j for transverse electric (TE) and transverse magnetic (TM) waves can be calculated from

$$R_{ij}^{\mathrm{TE}} = \frac{Z_j \cos\theta_i - Z_i \cos\theta_j}{Z_j \cos\theta_i + Z_i \cos\theta_j}\,, \tag{5}$$

$$R_{ij}^{\mathrm{TM}} = \frac{Z_i \cos\theta_i - Z_j \cos\theta_j}{Z_i \cos\theta_i + Z_j \cos\theta_j}\,. \tag{6}$$

The transmission coefficients from layer i to j are

$$T_{ij}^{\mathrm{TE}} = 1 + R_{ij}^{\mathrm{TE}}\,, \tag{7}$$

$$T_{ij}^{\mathrm{TM}} = 1 + R_{ij}^{\mathrm{TM}}\,. \tag{8}$$

3.4 Spatial Resolution

The spatial resolution of LPR is the primary consideration for design, and consists of two components: the radial resolution which indicates the limiting thickness of a layer and the lateral resolution which indicates the limiting size of a target. The radial resolution derived from (Jol 2009) is

$$\Delta r \geq \frac{Wv}{4} = \frac{v}{4B} = \frac{v}{4f_{\mathrm{c}}}\,, \tag{9}$$

where the pulse width W is directly related to the bandwidth B, which is also related to the center frequency f_c.

The lateral resolution can be calculated from

$$\Delta l \geq \sqrt{\frac{Wvr}{2}}\,, \tag{10}$$

where r is the distance to the target.

3.5 Dielectric Constant of Lunar Regolith

The dielectric constant, which is one of the most fundamental electromagnetic parameters, greatly affects the interpretation of data from LPR. The range resolution depends on the real part of the dielectric constant and the LPR bandwidth, whereas the penetration depth depends on the complex dielectric constant describing lunar subsurface materials and EM wave frequencies.

Wang & Yu (2010) described the bulk density of regolith at the lunar surface as follows

$$\rho_0 = \frac{\log \varepsilon_0'}{\log 1.919}\,, \tag{11}$$

where ε_0' represents the dielectric constant of a vacuum. Hence, for a given depth of lunar regolith h, the bulk density can be expressed as

$$\rho(h) = \rho_0 + 0.62 + \frac{11.136}{h + 18}\,. \tag{12}$$

The profile of the loss tangent of the regolith is modeled as

$$\tan\delta(h) = 10^{(0.44\rho(h) - 2.943)}\,. \tag{13}$$

Suppose the lunar subsurface is homogeneous, then the permittivity coefficient can be written as $\varepsilon = \varepsilon' + \varepsilon''$. The imaginary part of the permittivity coefficient is derived from

$$\varepsilon'' = \varepsilon' \tan\delta\,. \tag{14}$$

The lunar regolith is the top unconsolidated layer of fragmented, fine-grained, cohesive, clastic material. Regolith is composed of crystalline rock fragments, mineral fragments, breccia, aggregates held together with impact glass called agglutinates and glasses. The regolith samples that were returned from the US Apollo missions showed that the bulk component of regolith is a fine gray soil with a density ranging from about 1.3 g cm^{-3} to 1.92 g cm^{-3}, but the regolith also includes breccia and rock fragments from the local bedrock, in which the real part of the permittivity coefficient varies from 2.3 to 3.5, and the loss tangent is in the range 0.005 to 0.009. The permittivity coefficient of the mare basalts can have values from of 6.6 to 8.6, and the loss tangent varies between 0.009 and 0.016 (Heiken et al. 1991).

Figure 2 shows depth profiles of several indices related to the maturity of lunar regolith, which were derived from samples returned by the Apollo missions. In general, the indicators of maturity gradually increase in the in range $0 \sim 50$ cm deep, and tend to have little fluctuation deeper than 100 cm.

4 SIMULATED DEMONSTRATION OF LPR ECHO

The GprMax2D software suite was adopted to simulate radar images. We assume that the electrical conductivity is sufficiently low and the attenuation coefficient of the echoes is negligible in the present analysis.

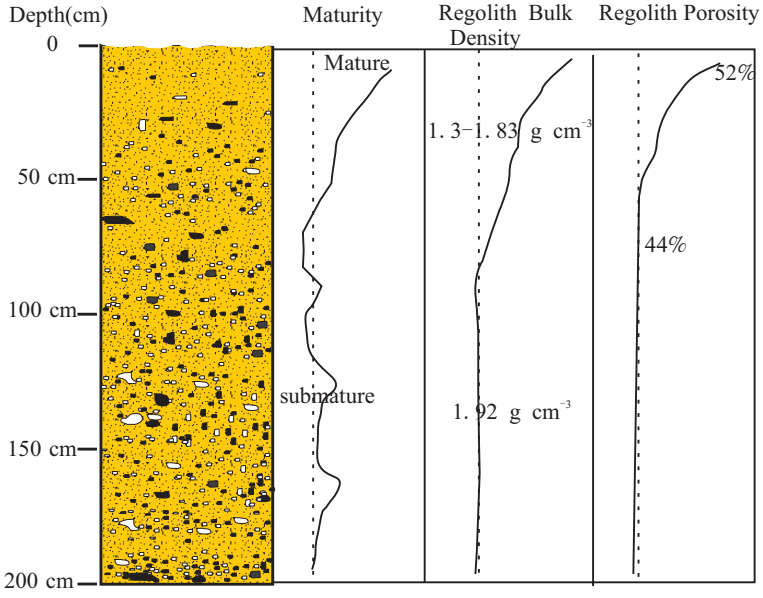

Fig. 2 The depth profiles of several maturity indices.

4.1 Excitation of the Waveform

The excitation source is chosen to be a differentiated Gaussian pulse, which has no DC components. The time domain waveform of the Gaussian pulse source is

$$E_{\mathrm{ewt}}(t) = \frac{t - t_0}{\tau} \exp\left[-\frac{4\pi(t - t_0)^2}{\tau^2}\right], \tag{15}$$

where t_0 is the time delay and the constant τ is the width of the pulse. Therefore, its frequency spectrum is

$$E_{\mathrm{ewf}}(f) = \frac{j\tau^2 f}{16\pi} \exp\left[-j2\pi f t_0 - \frac{\pi f \tau^2}{4}\right]. \tag{16}$$

The source waveform is a Ricker wavelet centered at 500 MHz in the simulation.

4.2 A-Scope Echo Simulation

For comparison, simulations of the radar echo were modeled as two cases. As shown in Figure 3 (left), Model 1 is for a multilayer regolith structure. It is ordered from top to bottom such that the vacuum layer has a thickness of 1 m, the regolith layer has a thickness of 7 m and there is a 2 m thick bedrock layer with a relative dielectric permittivity equal to 6. In addition, the regolith layer is subdivided into seven uniform sublayers, with variations in relative dielectric permittivity from 2.3∼3.5 with an increment of 0.2 for each sublayer.

Model 2 is for three-layer regolith (Zhang et al. 2014), as illustrated in Figure 3 (right). The regolith layer is modeled as a single homogeneous medium with a thickness of 7 m and a relative dielectric permittivity of 2.8. This value is chosen such that the time spent for the radio wave to propagate through this layer is equal to the time that is spent inside the seven sublayers of the regolith for Model 1. The value of relative dielectric permittivity for the bedrock layer is chosen as 6 in both cases. The mesh is set to 5×5 mm in a simulation domain of 10×10 m. The computation time step is 23.58 ps and the time widows are 120 ns.

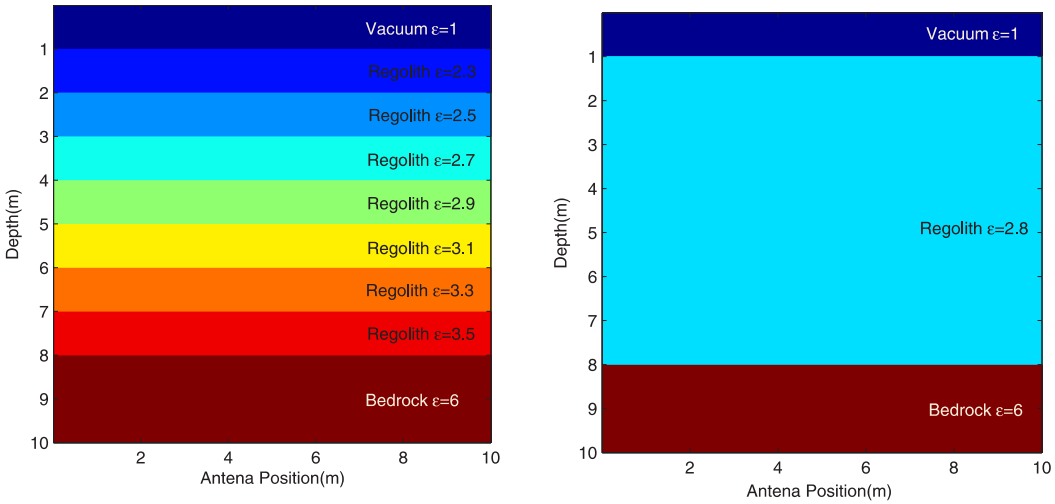

Fig. 3 The regolith model. *Left*: regolith Model 1: the multilayer model. *Right*: regolith Model 2: the three-layer model.

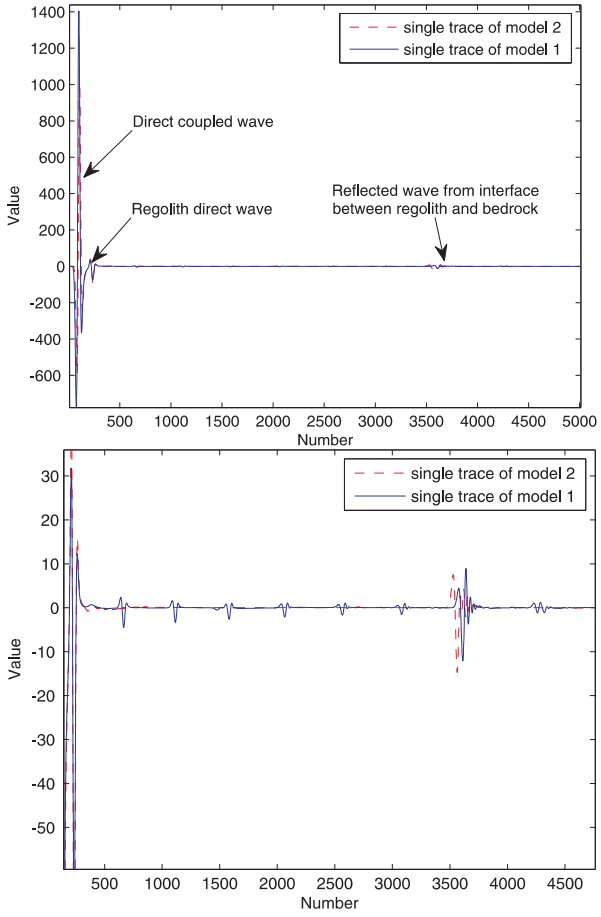

Fig. 4 The simulated LPR echoes from the regolith model. *Top*: The simulated LPR echoes. *Bottom*: An enlarged view that shows details of the wave that is reflected from the interface.

For the LPR discussed in this paper, there is a 20 cm difference in height between the radar antenna for the second channel and the surface of the regolith with a 10 cm spacing between the transmitting antenna and receiving antenna due to their mounting position on the rover. Figure 4 (top) shows two simulated single traces for Model 1 and 2, in which the blue solid curve represents the result from Model 1 and the red dashed curve represents the result of Model 2.

There are three types of EM waves that appear in both cases which are the direct coupled wave caused by the downward propagation from the transmitting antenna and receiving antenna, the direct wave from the interface between the vacuum and the regolith and the reflected wave from the interface between the regolith and the bedrock. However, by comparing Figure 4 (bottom) with Figure 4 (top) the transitions between sublayers in the regolith appear as six small reflections traced by the solid blue line. These are not present in Model 2 which only has vacuum/regolith interfaces. Moreover, for Model 1, the amplitude of the seventh reflection is higher than other reflections because of a major difference in the type of medium.

4.3 B-scan Simulation

Figure 5 shows the simulated results of a B-scan using LPR. This is used to investigate the depth as derived from the time delay of Model 1 and Model 2. It is clear that there are more than seven reflections in Figure 5 (left), which is also more than what is shown in Figure 5 (right), corresponding to the seven sublayer transitions inside the regolith layer using Model 1. Figure 5 (left) suggests that there is a ramp-shaped waveform that appears in the time delay range of 85$\sim$105 ns, meaning there is a fake layer arising from a wave that repeatedly reflects between the sublayer-interfaces. In addition, there are wave-absorbing boundaries. The echoes from the bedrock are both obvious, nevertheless the reflections in Figure 5 (right) are much weaker because of the small changes in dielectric constant.

4.4 Rock in Regolith Simulation

We have simulated rock reflections in a model that incorporates a homogeneous medium, as depicted in Figures 6 and 7. The mesh was set to 5 mm$\times$5 mm in a domain of 30 m$\times$5 m. Two cases were considered: in Model 3, five round rocks were placed in the regolith at a depth of 3 m and the distance between each rock is 5 m. The radii of the rocks are 4, 8, 12, 16 and 20 cm respectively. In Model 4, five round rocks with the same size are placed in the regolith at different depths, which are 3.5, 3, 2.5, 2 and 1.5 m respectively. The relative dielectric permittivity of the regolith is equal to 2.8 and the relative dielectric permittivity of the rocks is 7.

Figure 8 shows the simulated B-scan from regolith Model 3. It can be seen that two hyperbolic echoes emerge from the upper and lower interfaces of the rocks and regolith. As the spherical radius of the rock increases, the time delay between two echoes also gradually increases. The first group of echos from the left has just one layer, since the size of the rock is close to the limiting resolution of the radar. Figure 9 shows the simulated B-scan from regolith using Model 4. It can be seen that with spherical increases in rock depth, the width of the hyperbolic echo is also gradually increasing.

5 COMPARATIVE ANALYSIS AND DISCUSSION

CE-3 was launched on 2013 December 2 and it successfully landed on the Moon. The landing place is at 44.1260N, 19.5014W in Mare Imbrium, as shown in Figure 10, about 40 km south of the crater Laplace F (Zhao et al. 2014). The Yutu rover was successfully deployed from the lander and touched the lunar surface on 2013 December 14 (Ip et al. 2014).

Figure 11 shows simulated images of the B-scan for the detection route which was produced by echo signals from LPR observation data received at the surface from distinct points N105 to N208 collected during several normal working periods of the rover (Su et al. 2014). It can be seen

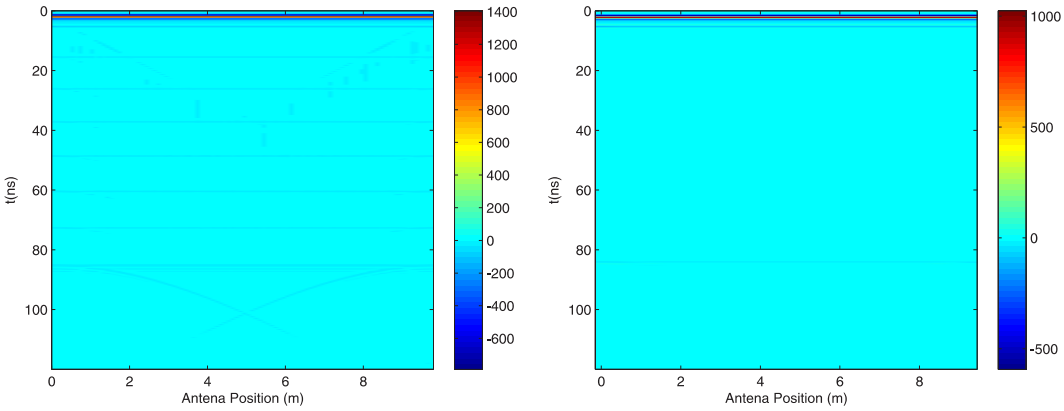

Fig. 5 The simulated B-scan from the regolith model. *Left*: The simulated B-scan of Model 1. *Right*: The simulated B-scan of Model 2.

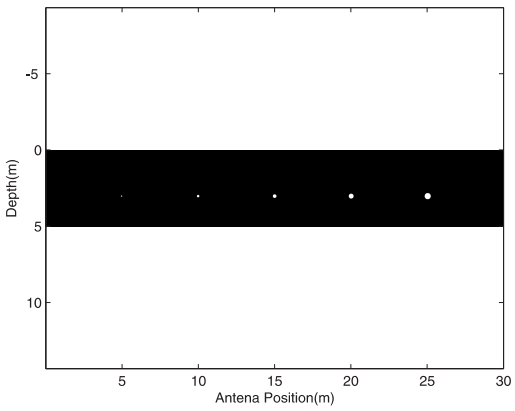

Fig. 6 The regolith as determined with Model 3.

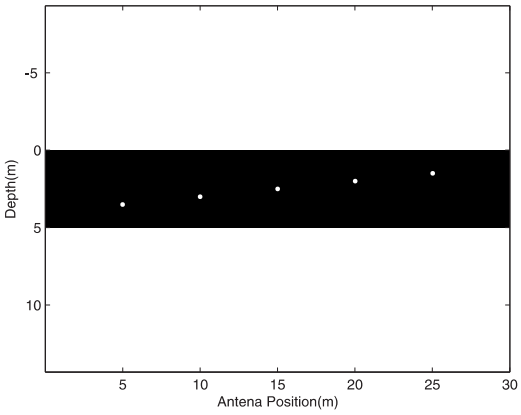

Fig. 7 The regolith as determined with Model 4.

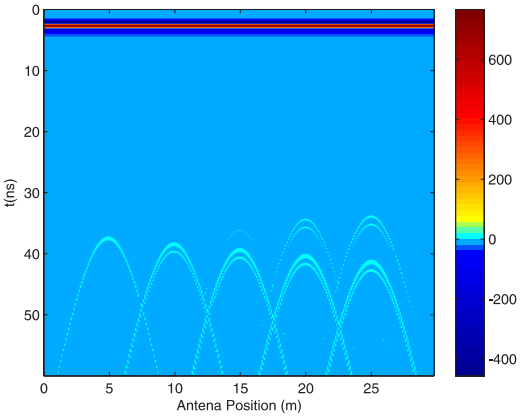

Fig. 8 The simulated B-scan from the regolith as determined with Model 3.

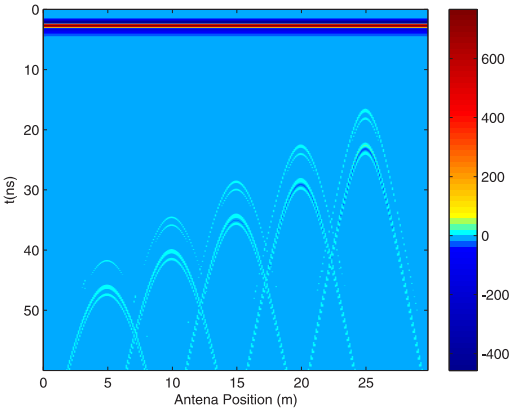

Fig. 9 The simulated B-scan from the regolith as determined with Model 4.

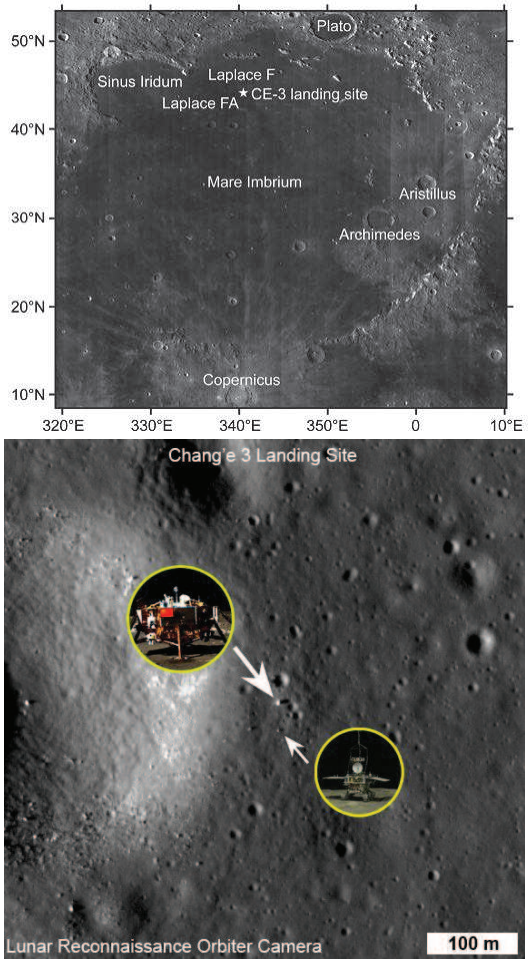

Fig. 10 Location of the CE-3 landing site. *Top*: Location of the CE-3 landing site within Mare Imbrium (Zhao et al. 2014). *Bottom*: A photo of the CE-3 landing site taken by a camera mounted on the LRO.

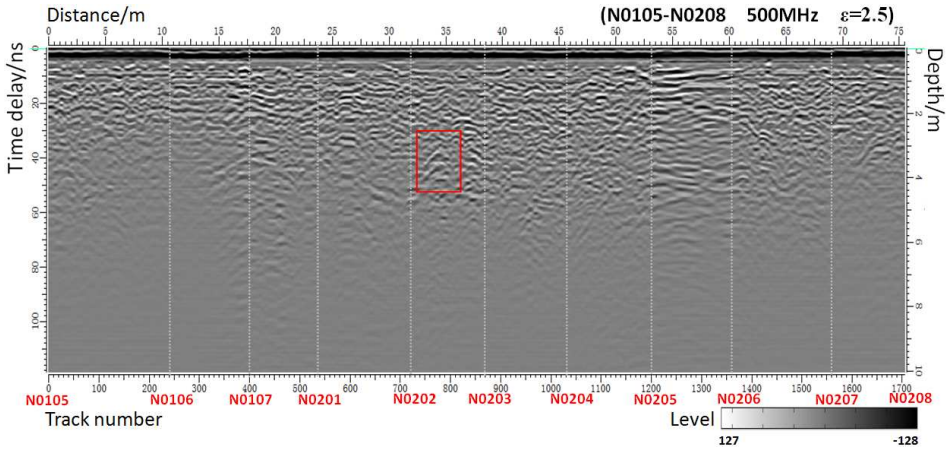

Fig. 11 The B-scan images of LPR.

that many reflections took place with a range of time delays between 0∼80 ns. There are relatively obvious boundaries found at about 50 ns, which indicate that there are many layers present in the regolith. This is consistent with the simulation presented in Section 4. In that simulation, the dielectric permittivity of the regolith was set to be 2.5 and the thickness was calculated to be 4.74 m. The calculated result is roughly in accordance with values published in previous studies (Heiken et al. 1991; Shkuratov & Bondarenko 2001; Kobayashi et al. 2012). A distinct 2-layer hyperbolic echo appears at 40 ns in region N202∼N203 as marked in the figure. The time delay between the upper and lower echo is approximately 5 ns, and the width of the echo is about 3 m. By comparing with the simulated radar B-scan images based on the model, it can be inferred that there may exist a rock at a depth of 3 m in that region, with a radius of about 15 cm. More interpretation of this image will be presented in another paper.

6 CONCLUSIONS

A simple lunar subsurface structure model for an area of mare basalt is established according to the principle of LPR, and a description of preliminary lunar landings and photographic investigations are presented. The model includes a vacuum, regolith layer, sputtered layer and bedrock. The dielectric constant of lunar regolith, the velocity of propagation, the reflection, refraction and transmission at interfaces, the resolution and the scattering attenuation are discussed. The A-scope and B-scan images based on a typical vacuum-regolith-bedrock model and the multilayer model are simulated. The influences of separate rocks placed in the model on the B-scan at different positions and sizes are also analyzed. The actual thickness of regolith for a certain detection route around the landing site of CE-3 is estimated to be about 4∼8 m which is consistent with previous research. This should help specialists in this field better understand the nature of the Moon.

Acknowledgements This work was supported by the National Natural Science Foundation of China (Grant Nos. 11173038 and 11203046), and by the Young Researcher Grant of National Astronomical Observatories, Chinese Academy of Sciences.

References

Bourgeois, J. M., & Smith, G. S. 1996, IEEE Transactions on Geoscience and Remote Sensing, 34, 36
Carcione, J. M. 1996, Geophysics, 61, 1664
Daniels, D. 2004, Ground Penetrating Radar, (2nd edn.; London: The Institution of Electrical Engineers)
Fa, W., & Jin, Y.-Q. 2007, Journal of Geophysical Research (Planets), 112, 5003
Fa, W., & Jin, Y.-Q. 2010a, Icarus, 207, 605
Fa, W.-Z., & Jin, Y.-Q. 2010b, Science China: Earth Sciences, 53, 1043
Fang, G.-Y., Zhou, B., Ji, Y.-C., et al. 2014, RAA (Research in Astronomy and Astrophysics), 14, 1607
Giannopoulos, A. 2005, Construction and Building Materials, 19, 755
Heiken, G. H., Vaniman, D. T., & French, B. M. 1991, Lunar Sourcebook – A User's Guide to the Moon (Cambridge: Cambridge Univ. Press)
Ip, W.-H., Yan, J., Li, C.-L., & Ouyang, Z.-Y., 2014, RAA (Research in Astronomy and Astrophysics), 14, 1511
Jol, H. M. 2009, Ground Penetrating Radar: Theory and Applications (Amsterdam: Elsevier Science)
Kobayashi, T., Kim, J. H., Lee, S. R., Araki, H., & Ono, T. 2010, IEEE Geoscience and Remote Sensing Letters, 7, 435
Kobayashi, T., Lee, S. R., & Ping, J.-S. 2012, in 14th International Conference on Ground Penetrating Radar (IEEE), 913
Kobayashi, T., Oya, H., & Ono, T. 2002a, Earth, Planets, and Space, 54, 973
Kobayashi, T., Oya, H., & Ono, T. 2002b, Earth, Planets, and Space, 54, 983
Nozette, S., Spudis, P., Bussey, B., et al. 2010, Space Sci. Rev., 150, 285

Ono, T., Kumamoto, A., Nakagawa, H., et al. 2009, Science, 323, 909
Rejiba, F., Camerlynck, C., & Mechler, P. 2003, Radio Science, 38, 1005
Sanintenoy, A., Schneider, S., & Tucholka, P. 2008, Vadose Zone Journal, 7, 208
Shkuratov, Y. G., & Bondarenko, N. V. 2001, Icarus, 149, 329
Spudis, P. D., Bussey, D. B. J., Baloga, S. M., et al. 2010, Geophys. Res. Lett., 37, 6204
Su, Y., Fang, G.-Y., Feng, J.-Q., et al. 2014, RAA (Research in Astronomy and Astrophysics), 14, 1623
Wang, Z.-Z., Li, Y., Jian, J.-S., & Li, D.-H. 2010, Science China Earth Sciences, 53, 1365
Zhang, H.-B., Zheng, L., Su, Y., et al. 2014, RAA (Research in Astronomy and Astrophysics), 14, 1633
Zhao, J., Huang, J., Qiao, L., et al. 2014, Science China Physics, Mechanics and Astronomy, 57, 569